From Jurassic rifting to Cretaceous subduction in NW Iranian Azerbaijan: geochronological and geochemical signals from granitoids

Journal Article

Author(s):
Lechmann, Anna; Burg, Jean-Pierre; Ulmer, Peter; Mohammadi, Ali; Guillong, Marcel; Faridi, Mohammad

Publication date:
2018-12

Permanent link:
https://doi.org/10.3929/ethz-b-000307643

Originally published in:
Contributions to Mineralogy and Petrology 173(12), https://doi.org/10.1007/s00410-018-1532-8

Contributions to Mineralogy and Petrology (2018) 173:102
https://doi.org/10.1007/s00410-018-1532-8

ORIGINAL PAPER

From Jurassic rifting to Cretaceous subduction in NW Iranian Azerbaijan: geochronological and geochemical signals from granitoids

Anna Lechmann[1] · Jean-Pierre Burg[1] · Peter Ulmer[1] · Ali Mohammadi[1] · Marcel Guillong[1] · Mohammad Faridi[2]

Received: 1 June 2018 / Accepted: 12 November 2018

Abstract

Previous interpretations of a Jurassic subduction in Iran were based on trace element classification diagrams for granitoids, but their reliability is questionable, underscored by modern examples of continental break-up zones such as the Baja California. We present new field observations, bulk rock geochemistry, Sr and Nd isotope analyses and U–Pb zircon geochronology to assess the age and tectonic setting of previously undated intermediate to felsic magmatic rocks cropping out in the Precambrian basement of NW Iranian Azerbaijan. The geochronology revealed an uneven distribution in space and time: Late Jurassic (159–154 Ma) intrusions and dikes are alkaline to calc-alkaline. Their melt source is mantle dominated with a distinct continental contribution disclosed by radiogenic isotopes and abundant inherited zircon cores. Mid-Cretaceous (112–96 Ma) plutonic bodies and associated volcanic rocks occur only to the east of the major Siah Cheshmeh–Khoy Fault. They have geochemical signatures typical of a metasomatized mantle. In consistence with the sedimentation history of the area, our new interpretation attributes the Late Jurassic magmatism to thinning of a continental lithosphere in a rift-related setting. Mid-Cretaceous magmatism was produced by oceanic subduction beneath the Central Iran continent. We interpret the 40-Ma age gap between the two magmatic episodes as the time of opening of the oceanic basin witnessed by the Khoy ophiolite in the study area.

Keywords NW Iran · Granitoids · Zircon geochronology · Jurassic rifting · Cretaceous subduction

Introduction

The Khoy ophiolite complex is located to the northwest of the city of Khoy, between the Sanandaj–Sirjan zone and the Central Iranian block (Fig. 1; e.g. Hassanzadeh and Wernicke 2016). The Khoy ophiolite represents a former oceanic basin (e.g. Khalatbari-Jafari et al. 2003) whose opening and closure remain disputed. Likewise, the setting of the Khoy ophiolite with respect to the other ophiolites of the Zagros fold belt (Fig. 1) remains debated. Closure of the Neo-Tethys Ocean and related seaways, and beginning of collision took place between Late Eocene/Oligocene and Early Miocene (e.g. Agard et al. 2005; Ballato et al. 2011; Okay et al. 2010; Vincent et al. 2005). Subduction along the northern margin of the Neo-Tethys below the Sanandaj–Sirjan zone is claimed to have started in latest Triassic to Early Jurassic forming a magmatic arc represented by Middle to Late Jurassic (150–175 Ma) intrusions (Fig. 1; Hassanzadeh and Wernicke 2016 and references therein).

Geological maps of the Khoy area report granitoid plutonic bodies with subordinate volcanic rocks. These granitoids are not ascribed to any geological setting due to scarce age constraints. This study presents 14 U–Pb zircon ages of granitoid rocks revealing two periods of magmatic activity: Late Jurassic (159–154 Ma) and Middle Cretaceous (112–96 Ma). The active Siah Cheshmeh–Khoy right lateral strike-slip fault cuts the region into two parts (Fig. 2). The Late Jurassic intrusions and dikes occur on both sides of the fault. Conversely, Cretaceous plutonic bodies occur only in the Central Iranian block on the northeast side of the fault. Fieldwork, petrological and geochemical results point to an

Communicated by Jochen Hoefs.

Electronic supplementary material The online version of this article (https://doi.org/10.1007/s00410-018-1532-8) contains supplementary material, which is available to authorized users.

✉ Anna Lechmann
anna_lechmann@hotmail.com

[1] Department of Earth Sciences, ETH Zurich, 8092 Zurich, Switzerland

[2] Geological Survey of Iran, Tabriz 5133-4359, Iran

Published online: 20 November 2018

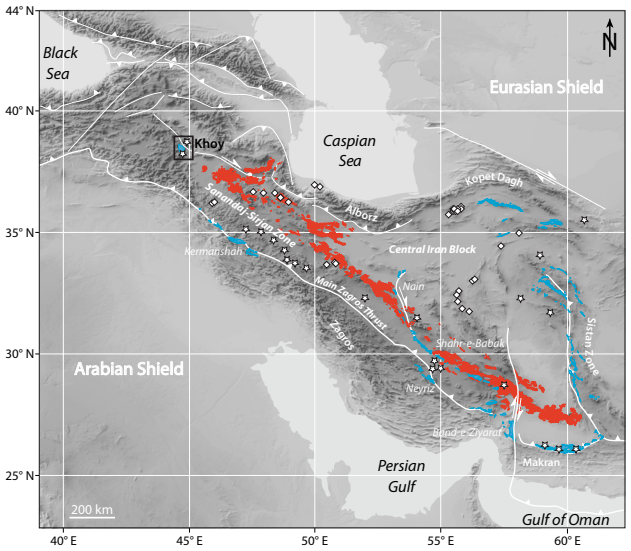

Fig. 1 Tectonic setting of Iran with Tethys ophiolite complexes (blue), the Urumieh–Dokhtar Magmatic Arc (UDMA; red), Neoproterozoic to Cambrian crystalline basement (diamonds) and Jurassic granitoids (stars). See text for references. Framed: study area. Background: shaded relief map ETOPO1 (http://www.ngdc.noaa.gov/mgg/global/relief/ETOPO1)

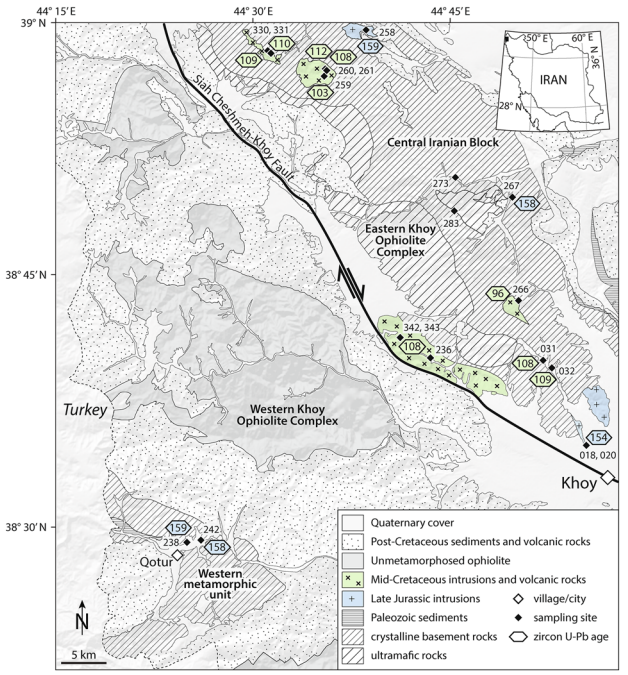

Fig. 2 Simplified geological map of the Khoy area with sampling locations and zircon U–Pb ages

extensional event during the Late Jurassic, when mantle-derived magmas intruded a thinned continental lithosphere. This extensional event led to the formation of the Khoy oceanic lithosphere between the Sanandaj–Sirjan zone and the Central Iranian block. Closure of this basin started in the Mid-Cretaceous forming a calc-alkaline magmatic arc along the continental margin of the Central Iran block. Therefore, the active Siah Cheshmeh–Khoy Fault reactivates the former site of subduction.

Geological setting

The Khoy area is located in northwest Iran (Fig. 1). Field work was carried out using maps published by the Geological Survey of Iran at 1:250,000 (Khoy: Haghipour et al. 1978) and 1:100,000 scales (Dizaj: Amini et al. 1993; Khoy:; Radfar et al. 1993; Qotur:; Khodabandeh et al. 2002a, Salmas: b). The study area is subdivided into three major NW–SE trending units, from northeast to southwest (Fig. 2): (1) the Central Iranian block (CIB), (2) the Khoy ophiolite complex (KOC) and (3) the western metamorphic unit (WMU), which extends into Turkey and the East Anatolian Plateau (Khalatbari-Jafari et al. 2003). The three units are characterized by Mesozoic–Cenozoic southwestward thrusting (Khalatbari-Jafari et al. 2003). Several NW–SE trending dextral strike-slip faults have sliced these units and dominate the recent tectonic activity (Karakhanian et al. 2004). However, original lithological contacts are preserved in places.

The CIB belongs, like the Sanandaj–Sirjan zone and the Alborz Mountains, to the Late Neoproterozoic to Early Cambrian continental basement (Azizi et al. 2011; Guest et al. 2006; Hassanzadeh et al. 2008; Lam 2002; Ramezani and Tucker 2003; Samani et al. 1994; Verdel et al. 2007). Permo-Triassic platform limestones with Eurasian fauna unconformably cover the gneisses and granitoids of this basement (Berberian and King 1981; Stöcklin 1968). Paleogeographic reconstructions show that the CIB rifted from the northern margin of Gondwana during the Permian to Mesozoic opening of the Neo-Tethys (e.g. Stampfli 2000; Stöcklin 1968).

The KOC is subdivided into the eastern (EKOC) and western (WKOC) Khoy ophiolite complex (Fig. 2). The EKOC was defined as a meta-ophiolitic unit with tectonic slices of ultramafitites and amphibolites, micaschists, marbles and greenschist-metamorphic metabasic rocks (Khalatbari-Jafari et al. 2003). $^{40}K/^{40}Ar$ amphibole ages of amphibolites range from 189 to 102 Ma, loosely suggesting a pre-Jurassic primary magmatic age (Khalatbari-Jafari et al. 2004). $^{40}Ar/^{39}Ar$ age determination on hornblendes of amphibolites consistently yielded two age groups: 159–155 and 104–112 (Ghazi et al. 2001, 2003; Pessagno et al. 2005). Based on U–Pb zircon and Rb–Sr mineral isochron dating, Azizi et al. (2011) determined a Neoproterozoic crystallization age (< 550 Ma) for metagranites and metabasalts that would have experienced a metamorphic event < 146 Ma ago. The Neoproterozoic

age is consistent with other ages measured on CIB rocks (Fig. 1; Hassanzadeh et al. 2008; Ramezani and Tucker 2003), suggesting that the ultramafic and mafic EKOC is part of the CIB. The WKOC is separated from the CIB and the EKOC by the active right lateral Siah Cheshmeh–Khoy strike-slip fault (Djamour et al. 2011), and post-Cretaceous sediments and volcanics. The WKOC is an almost complete, non-metamorphic ophiolitic sequence from harzburgitic mantle rocks to layered gabbros, pillow lavas, sheet flows and Late Cretaceous (Turonian to Campanian) pelagic limestones (Khalatbari-Jafari et al. 2003).

The western metamorphic unit (WMU) is composed of altered ultramafic rocks, gabbros, amphibolites and greenschist facies metabasic rocks covered by Permian dolomites and limestones (Khodabandeh et al. 2002a). No detailed analytical work has been performed on the WMU to date, but the unit is interpreted as the northwestern extension of the Sanandaj–Sirjan zone (Hassanzadeh and Wernicke 2016). Across the border, on the Turkish side, ophiolites and ophiolitic mélanges of the East Anatolian Plateau, covered extensively with Neogene and Quaternary volcanics and sediments, are connecting the Izmir–Ankara–Erzincan suture with the Zagros suture (Şengör 1990; Topuz et al. 2017).

Analytical methods

Bulk rock analyses were acquired using XRF and LA–ICP–MS at ETH Zurich. For U–Pb ages, zircons were separated, mounted and analyzed by LA–ICP–MS at ETH Zurich. Crystallization ages were calculated using weighted mean $^{206}Pb/^{238}U$ ages of concordant measurements using Isoplot (Ludwig 2012) with 95% confidence and total uncertainties, including quadratically propagated external error as suggested in Horstwood et al. (2016). The MSWD is calculated based on internal uncertainty. High MSWD values are assumed to be due to either prolonged crystallization, contamination, open system behaviour, such as Pb loss or heterogeneity. Details of data handling are given in supplement S1. Solution ICP–MS and bulk rock radiogenic Sr and Nd isotope analyses were carried out at the Victoria University of Wellington, New Zealand. Analytical methods are described in supplement S1.

Sampling

The dated rocks were sampled in the three CIB, EKOC and WMU units (Fig. 2). The kilometer-sized plutonic bodies in the CIB (Fig. 3a) are dominantly medium- to

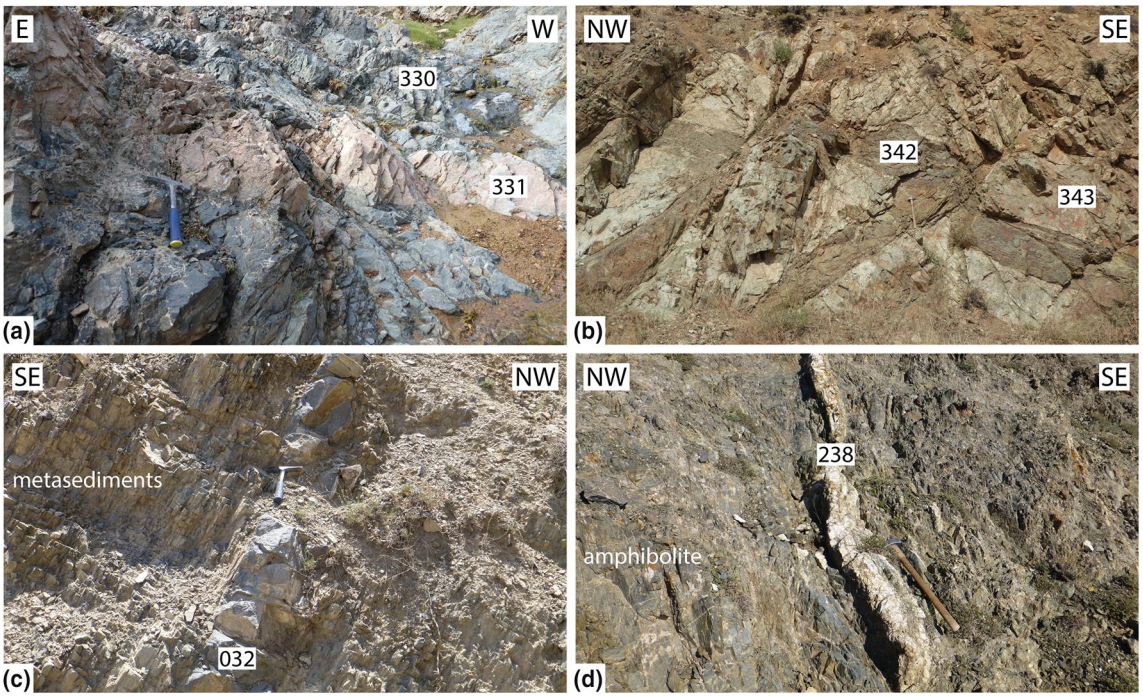

Fig. 3 Field photographs of Khoy granitoids. **a** Granite 331 intruding monzodiorite 330 as part of a km-scale intrusion in the north of the EKOC (38°58′20.4″N, 044°31′00.4″E). **b** Monzogabbroic dike 342 crosscutting rhyodacite 343 between the EKOC and the WKOC (38°41′09.3″N, 044°41′08.8″E). **c** Granitic dike 032 intruding metasediments of the EKOC (38°39′11.5″N, 044°52′45.0″E). **d** Trondhjemite dike 238 intruding amphibolites of the WMU (38°28′54.1″N, 044°24′30.5″E). Sample locations in Fig. 2

Table 1 Sampling site coordinates, U–Pb zircon ages and petrography (mineral assemblage and texture)

Sample number	Coordinates	$^{206}Pb/^{238}U$ (Ma) and assumed ages	Name according to Le Maitre and Barker[b]	Mineral assemblage (primary)	Alteration products
018	N38°34′59.3″ E44°55′22.4″	Jurassic	Trondhjemite	pl, qz, ms, aln	chl, ep, prh
020	N38°34′46.7″ E44°55′27.0″	153.9 ± 3.3	Granite	qz, kfs, pl, bt, ms, aln, zrn	ep, chl
031	N38°40′06.8″ E44°51′41.7″	108.1 ± 2.1	Granodiorite (dike)	qz, kfs, pl, ms, zrn	ep
032	N38°39′11.5″ E44°52′45.0″	109.1 ± 1.7	Granite (dike)	qz, kfs, pl, amp, ttn, mag, zrn	chl, ep
236	N38°39′57.8″ E44°43′21.1″	Cretaceous	Monzogabbro	cpx, pl, qz, ap, opq	chl, ep, cb
238	N38°28′54.1″ E44°24′30.5″	158.6 ± 2.5	Trondhjemite (dike)	qz, pl, zrn	cb
242	N38°29′11.4″ E44°26′08.9″	157.7 ± 2.9	Monzodiorite (dike)	zrn	ep, ms, chl, bt, prh, ttn
258	N38°59′34.5″ E44°38′21.2″	158.9 ± 2.5	Granodiorite	qz, kfs, pl, amp, bt, ms, ap, opq, zrn	chl, cb
259	N38°56′50.1″ E44°35′19.4″	102.6 ± 2.9	Granite[a]	qz, kfs, pl, bt, ms, opq, zrn	chl, ep
260	N38°57′17.6″ E44°35′15.2″	108.4 ± 1.7	Qz-Monzodiorite	pl, kfs, qz, bt, amp, ap, zrn	ep
261	N38°57′18.9″ E44°35′14.3″	111.5 ± 4.7	Granite (dike)	qz, kfs, pl, opq, zrn	ep
266	N38°43′54.2″ E44°51′41.2″	96.2 ± 1.6	Granodiorite	qz, pl, ms, zo, zrn	
267	N38°49′39.0″ E44°49′39.6″	158.3 ± 2.6	Diorite (dike)	pl, amp, ttn, ap, ms, opq, zrn	chl, ep, cb
273	N38°50′43.9″ E44°45′23.4″	Jurassic	Monzodiorite (dike)	kfs, pl, qz, amp, ttn, ap, aln, opq	chl, ep, cb
283	N38°48′41.4″ E44°45′28.8″	Jurassic	Diorite (dike)	pl, ms	
330	N38°58′20.4″ E44°31′00.4″	109.2 ± 1.7	Monzodiorite	pl, kfs, amp, bt, ttn, ap, opq, zrn	ep
331	N38°58′20.4″ E44°31′00.4″	110.7 ± 2.8	Granite	kfs, qz, pl, ttn, opq, zrn	chl
342	N38°41′11.2″ E44°41′04.9″	Cretaceous	Monzogabbro (dike)	pl, cpx, ol?, opq	chl, ep, prh
343	N38°41′09.3″ E44°41′08.8″	107.7 ± 1.7	Rhyodacite (volcanic)	qz, kfs, pl, opq, zrn	chl, ep, ms

Mineral abbreviations according to Whitney and Evans (2010)

[a]No bulk rock chemistry, name from petrographic observations only

[b]Names of the rocks derived from observed and normative mineralogy (CIPW) according to Le Maitre et al. (2002) and Barker (1979)

coarse-grained granitoids with equigranular to porphyritic texture. EKOC monzogabbros are altered to a greenschist facies assemblage but preserved the original magmatic texture. Subvolcanic dikes with doleritic texture and rhyodacites are scarce (Fig. 3b). NNE–SSW to NE–SW striking decimeter- to meter-thick fine-grained holocrystalline granitic dikes with undeformed to foliated porphyritic texture intruded the CIB and the EKOC (Fig. 3c). In the WMU, large plutonic bodies are absent but felsic dikes similar in appearance and orientation to the CIB and EKOC dikes are common (Fig. 3d).

Petrography

Thin sections have been studied under the optical microscope to define the mineralogy and rock texture (Table 1). Starting from felsic to mafic compositions:

The felsic samples are holocrystalline and contain quartz, alkali feldspar and plagioclase as major constituents, all with anhedral to subhedral crystal habit (Fig. 4a, b). The samples are generally fresh but show indices of low-temperature metamorphism with chlorite, epidote, prehnite and carbonate veinlets. Quartz grains show undulose extinction and a consertal intergrowth texture. K-feldspars often show simple or cross-hatched twinning

and perthitic exsolution lamellae. Plagioclase grains are characterized by polysynthetic twinning. Biotite, muscovite, amphibole, zircon, apatite, titanite, allanite and iron oxides are accessory minerals. Anhedral grains of chlorite are related to biotite alteration. Sample 283 is a dioritic dike (Fig. 4c). Sample 343 is a hypocrystalline porphyritic rhyodacite with rounded phenocrysts of quartz, K-feldspar and plagioclase in a fine-grained matrix of the same composition. Quartz shows typical resorption embayments (Fig. 4d).

Intermediate, holocrystalline samples are dominated by anhedral to subhedral plagioclase, K-feldspar with minor to medium amounts of anhedral quartz, amphibole and biotite (Fig. 4e). Plagioclase has polysynthetic twinning, quartz undulose extinction and alkali feldspar is recognized by simple twinning. Accessory minerals are zircon, apatite, titanite, muscovite, allanite and opaques. The samples are fine to medium grained.

Monzogabbros are holocrystalline and contain plagioclase and clinopyroxene as major constituents. Large apatite grains (~ 0.5 mm), skeletal Fe-Ti oxides and quartz are accessory minerals. Plagioclase grains are subhedral and partially to completely replaced by epidote and chlorite (saussuritized) or prehnite. Anhedral to subhedral clinopyroxenes have lamellar twinning; few grains are zoned. They occur as phenocrysts, occasionally as

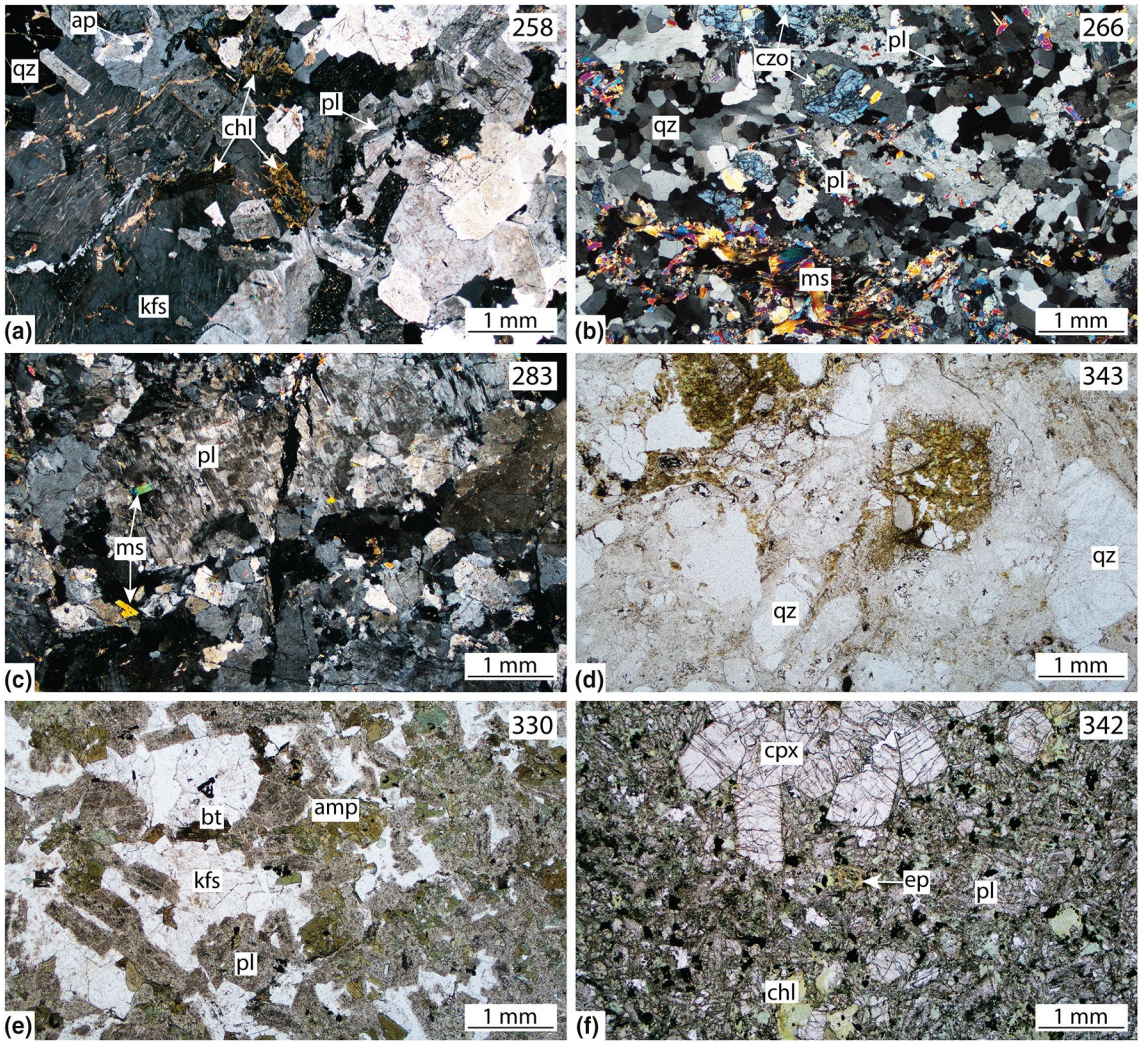

Fig. 4 Photomicrographs of granitoids and associated lithologies in the Khoy area. Mineral abbreviations after Whitney and Evans (2010). **a–c** Under cross-polarized light, **d–f** under plane-polarized light. **a** Granodiorite 258 (38°59′34.5″N, 44°38′21.2″E) with simple twinned alkali feldspar and perthitic exsolution lamellae. **b** Granodiorite 266 (38°43′54.2″N, 44°51′41.2″E) with large amount of clinozoisite and muscovite. **c** Diorite dike 283 (38°48′41.4″N, 44°45′28.8″E). **d** Rhyodacite 343 (38°41′09.3″N, 44°41′08.8″E) depicting resorption embayments in quartz. **e** Medium-grained monzodiorite 330 (38°58′20.4″N, 44°31′00.4″E) with saussuritized plagioclase, and anhedral biotite and amphibole. **f** Monzogabbroic dike 342 (38°41′11.2″N, 44°41′04.9″E) with glomerophyritic clinopyroxene phenocrysts in a fine-grained matrix of clinopyroxene and plagioclase. Sample locations given in Fig. 2

glomerophyritic assemblage or as fine grains in the matrix (Fig. 4f). Dispersion of the optic axes indicates augitic compositions. Magmatic olivine grains are replaced by fine-grained assemblages of chlorite and epidote. Calcite and chlorite veins are common.

Geochronology

Results of zircon geochronology, including statistics, are provided in Table 2. Cathodoluminescence (CL) images with laser-ablation sampling spots, metadata for LA–ICP–MS U–(Th)–Pb dating and the data of standards and measured samples are provided in supplements S2–S5.

The 14 dated intermediate to felsic samples yield two age groups (supplement S6): (1) Late Jurassic (159–154 Ma) and (2) Middle Cretaceous (112–96 Ma).

Late Jurassic (159–154 Ma)

Five Late Jurassic concordant ages were obtained (supplement S6), in the order of decreasing age: 158.9 ± 2.5 Ma (granodiorite 258), 158.6 ± 2.5 Ma (trondhjemite dike 238), 158.3 ± 2.6 Ma (dioritic dike 267), 157.7 ± 2.9 Ma (monzodioritic dike 242) and 153.9 ± 5.8 Ma (granite 020).

Monzodioritic dike 242 delivered only one zircon grain, which is statistically not relevant. However, sample 238 with an age of 158.6 ± 2.5 Ma and abundant concordant zircons confirms the presence of Late Jurassic dikes in the western metamorphic unit (WMU; Fig. 2).

Concordant $^{206}Pb/^{238}U$ Paleoproterozoic to Early Jurassic ages (175–2075 Ma, Table 2) are common in granites 020 and 258 (Fig. S6.1b), and in the dioritic dike 267. The old ages are attributed to assimilated zircon grains and inherited cores from the Precambrian basement. Trondhjemite dike 238 has ages between 169 and 180 Ma. Since the corresponding grains are very small (< 100 µm), ages may represent mixed rim-core ages. A few slightly younger ages were measured in dike 238 (146.0 ± 3.0 Ma and 146.4 ± 3.2 Ma) and 267 (149.8 ± 2.5). As the zircon grains were not chemically abraded, we assert that recent lead loss is responsible for these younger ages (Mattinson 2005).

Middle Cretaceous (112–96 Ma)

Nine Mid-Cretaceous concordant ages were obtained, in decreasing order (supplement S6): 111.5 ± 4.7 Ma (granitic dike 261), 110.7 ± 2.8 Ma (granite 331), 109.2 ± 1.7 Ma (monzodiorite 330), 109.1 ± 1.7 Ma (granitic dike 032), 108.4 ± 1.7 Ma (quartz-monzodiorite 260), 108.1 ± 2.1 Ma (granodioritic dike 031), 107.7 ± 1.7 Ma (rhyodacite 343), 102.6 ± 2.9 Ma (granite 259) and 96.2 ± 1.6 Ma (granodiorite 266).

Seven samples yielded older, dominantly Early Cretaceous ages (107–141 Ma, Table 2). These samples are characterized by fine-grained (< 200 µm) or complexly zoned zircons. We contend that these ages represent mixed rim-core ages due to ablating different age domains during measurement (Fig. S6.2f). Sample 031 additionally yielded assimilated grains and inherited cores with ages typical of the Paleozoic–Mesozoic cover of the Precambrian basement (180–415 Ma). Although we found zircon analyses with non-radiogenic Pb (inserts in Fig. S6.2), we did not apply a correction but, for simplicity, discarded all discordant analyses and used only measurements free of non-radiogenic Pb.

Geochemistry

17 samples are used to discuss major and trace element geochemistry. Results are listed in Table 3. Loss on ignition (LOI) values vary between 0.7 and 2.3 wt% for Jurassic samples and between 0.4 and 4.2 wt% for Cretaceous samples. This is consistent with the amount of hydrous minerals observed in thin section, which is higher for Cretaceous samples than for Jurassic samples. This disparity allowed allocating undated samples and used to discuss the bulk rock chemistry, to either Late Jurassic or Mid-Cretaceous granitoids. Subsolidus modification of mobile elements (e.g. Rb, Sr, K and Ba) is considered negligible as there is no systematic correlation with LOI.

Major and trace elements

SiO_2 contents range between 47 and 78 wt%. According to the AFM diagram (Fig. 5a), the samples are calc-alkaline and do not show any tholeiitic affinity. Since this diagram cannot discriminate calc-alkaline from alkaline affinity, the samples are further classified based on the total alkali vs. silica (TAS) diagram (Fig. 5b). This reveals that Jurassic samples have a distinctly more alkaline tendency than Cretaceous samples. Harker diagrams define different trends depending on the age of the sample with exception of potassium (K_2O = 0.3–7.3 wt%) which shows a wide scatter from low-K to high-K for both, Jurassic and Cretaceous samples (Fig. 6a).

Late Jurassic samples are depleted in $Fe_2O_3^{tot}$ (< 3 wt%) and TiO_2 (< 0.5 wt%) indicating early ilmenite fractionation (Fig. 6b, c). They can be subdivided into two groups (Fig. 5b): (1) alkaline and (2) sub-alkaline. Na_2O (6–10 wt%) and Al_2O_3 (18–21 wt%) contents are high for the alkaline samples and lower (Na_2O = 3–7 wt%; Al_2O_3 = 12–15 wt%) for the sub-alkaline granites (Fig. 6d, e). The samples are characterized by heterogeneous concentrations of K_2O

Table 2 External error corrected weighted mean $^{206}Pb/^{238}U$ ages and zircon description

Sample number	Number of measured grains	Number of measurements	Weighted $^{206}Pb/^{238}U$ age in Ma	n^a	MSWD	Internal uncertainty (±Ma)	Uncertainty incl. 1.5% external uncertainty (±Ma)	Zircon size (µm)	Aspect ratio	Inherited zircons and cores (Ma)	Recrystallized or altered zircons (Ma)
020	7	8	153.9	6	9.9	5.3	5.8	150	1–3.6	186, 216	–
031	50	53	108.1	43	13	1.3	2.1	70–200	1.5–3.5	121–130, 141, 177, 269, 290, 338, 415	–
										290, 338, 415	
032	140	153	109.1	125	5.2	0.6	1.7	80–200	1.5–4	120–129	–
238	75	84	158.6	74	6.8	0.8	2.5	100–330	1.5–4.5	169–180	146.0, 146.4
242	1	2	157.7	2	0.3	1.7	2.9	130	1.2	–	–
258	112	139	158.9	39	4.0	0.9	2.5	100–250	1.5–2.5	174–373, 390–457, 500–550, 720–790, 850, 1030, 2370	–
										720–790, 850, 1030, 2370	
259	64	80	102.6	7	5.0	2.4	2.9	80–200	1.5–4.5	107–110	–
260	130	131	108.4	104	5.1	0.4	1.7	100–330	1.5–4	114.1–115.7	–
261	41	42	111.5	5	18	4.4	4.7	60–130	1–2	–	–
266	7	7	96.2	7	1.5	0.8	1.6	n.d.	n.d.	n.d.	n.d.
267	84	97	158.3	49	5.4	1.0	2.6	120–330	1.5–3	168–173, 200–425, 500–557, 815, 921, 973, 2075	149.8
										815, 921, 973, 2075	
330	101	120	109.2	61	5.2	0.5	1.7	150–330	1.3–4	120–125	–
331	67	74	110.7	17	14	2.2	2.8	60–300	1.2–2.5	124.8, 124.9	–
343	68	76	107.7	65	3.5	0.5	1.7	60–160	1.2–2.5	113.1, 120.3	–

Total uncertainties, including internal and external uncertainties, have been calculated

[a] n = measurements considered for calculation of weighted mean age

n.d. No data

Table 3 Major (in wt%) and trace elements, and initial (*i*) Sr and Nd compositions of selected samples from Khoy, NW Iran

Sample	018	020[a]	031	032[a]	236	238[a]	242	258[a]	260[a]	266	267[a]	273	283	330	331[a]	342[a]	343[a]
SiO_2	63.21	72.60	77.95	74.92	46.73	72.17	56.62	66.45	56.34	73.27	59.28	61.37	63.74	60.59	75.44	48.89	71.94
TiO_2	0.05	0.22	0.33	0.31	1.09	0.03	0.30	0.50	1.00	0.11	0.37	0.05	0.05	0.72	0.15	1.04	0.34
Al_2O_3	21.59	14.02	10.93	12.43	19.18	14.30	21.82	15.18	17.82	15.01	21.68	18.46	20.83	15.31	12.47	14.40	14.33
Fe_2O_3[b]	0.46	1.47	1.42	0.88	9.05	0.27	2.09	2.75	7.28	1.05	2.21	0.77	0.31	6.10	1.32	9.46	3.38
MnO	0.01	0.03	0.01	0.01	0.13	0.01	0.03	0.05	0.11	0.03	0.02	0.03	0.00	0.11	0.01	0.15	0.03
MgO	0.36	0.38	0.89	0.18	4.25	0.17	1.89	1.08	3.04	0.31	0.90	0.28	1.16	3.33	0.12	7.90	0.89
CaO	5.07	1.61	2.17	0.73	11.11	2.45	4.92	2.23	6.56	2.09	4.44	4.11	1.25	4.64	0.33	9.43	0.39
Na_2O	6.80	3.85	2.94	2.01	2.65	6.98	6.20	4.83	3.84	4.37	7.94	7.80	9.94	4.84	3.92	2.19	3.36
K_2O	0.91	4.00	2.08	7.26	1.33	0.60	2.67	3.57	1.79	1.86	0.81	3.25	0.60	2.31	4.79	1.53	2.53
P_2O_5	0.024	0.054	0.070	0.023	0.173	0.007	0.176	0.175	0.225	0.074	0.117	0.087	0.043	0.119	0.019	0.184	0.056
Cr_2O_3	0.002	0.011	0.000	0.034	0.003	0.000	0.000	0.000	0.000	0.000	0.000	0.000	0.000	0.009	0.000	0.049	0.000
NiO	0.001	0.001	0.003	0.002	0.005	0.001	0.008	0.001	0.001	0.001	0.002	0.001	0.001	0.003	0.001	0.015	0.001
LOI[c]	1.04	0.74	0.88	0.55	4.18	2.29	2.01	2.02	1.42	1.00	1.09	2.22	1.05	1.11	0.45	4.15	2.24
Total	99.52	98.97	99.68	99.34	99.89	99.27	98.74	98.84	99.42	99.17	98.86	98.42	98.97	99.18	99.01	99.40	99.47
Mg#	0.64	0.36	0.58	0.31	0.51	0.59	0.67	0.46	0.48	0.39	0.47	0.45	0.89	0.55	0.17	0.65	0.37
Trace elements in ppm (bdl = below detection limit)																	
Sc	1.7	2.3	2.9	2.4	22.8	0.0	4.2	4.4	11.0	bdl	5.2	5.8	bdl	22.4	3.8	34.7	13.4
V	8.6	13.6	14.8	11.1	250	5.0	65.7	45.3	161	bdl	35.3	bdl	bdl	135	2.9	225	33.5
Cr	8.5	3.6	bdl	3.5	20.3	2.9	bdl	17.2	3.0	bdl	11.9	bdl	bdl	61.4	2.6	391	1.6
Co	5.5	15.4	11.1	4.4	33.0	2.2	15.7	6.8	19.8	4.4	9.2	4.1	4.3	19.0	3.1	43.2	5.5
Ni	10.6	30.5	21.2	8.7	42.4	4.1	60.6	8.1	4.7	8.7	15.7	4.9	10.5	23.5	7.2	125	5.6
Cu	5.9	0.7	14.5	9.1	116	1.8	1.8	8.2	20.7	2.7	12.4	30.0	bdl	21.8	2.1	74.6	1.7
Zn	bdl	35.9	9.3	11.3	60.8	3.1	15.8	53.1	86.5	bdl	26.6	bdl	bdl	92.3	21.9	87.1	55.6
Ga	14.5	18.7	9.0	12.8	14.7	8.9	17.7	23.1	19.4	13.1	20.5	14.6	17.5	19.4	18.5	16.3	16.7
Rb	15.6	75.5	57.9	244	24.8	4.6	62.2	84.7	40.3	60.4	10.5	65.3	17.7	72.0	166	39.0	72.0
Sr	712	176	206	152	481	184	875	751	234	516	1787	131	174	179	18.0	272	55.1
Y	2.8	4.8	4.8	10.0	16.5	0.1	8.0	12.6	22.8	3.1	5.0	10.8	6.4	30.1	39.7	17.9	30.0
Zr	60.2	153	169	149	57.1	1.4	235	43.1	29.6	76.3	5.8	33.1	55.3	201	88.9	85.4	115
Nb	0.7	12.8	4.4	5.9	4.4	0.1	15.9	23.5	12.5	6.8	2.2	5.5	3.2	21.1	38.0	7.3	5.8
Cs	0.3	0.5	0.7	4.6	0.6	0.1	1.7	0.8	1.2	1.1	0.4	2.0	0.4	1.5	1.6	2.2	2.5
Ba	510	789	257	348	216	75.5	1688	800	177	519	206	1003	268	287	255	517	393
La	5.5	27.9	10.6	11.4	8.0	0.2	44.2	43.5	20.8	16.5	2.3	26.3	19.6	25.9	41.5	9.6	14.6
Ce	11.3	46.8	18.3	20.2	16.8	0.4	70.8	76.3	45.8	27.7	5.6	42.7	38.1	53.9	81.6	19.3	30.7
Pr	1.4	4.6	1.8	2.3	2.3	0.0	6.2	8.0	5.5	3.0	0.8	3.9	3.6	6.1	8.7	2.5	3.8
Nd	5.6	14.9	6.9	8.6	10.2	0.2	17.8	29.4	22.5	8.6	3.5	12.0	13.5	23.2	30.4	11.4	16.3
Sm	1.4	2.5	1.4	2.0	2.5	0.0	1.6	5.0	5.0	1.7	1.0	bdl	2.1	3.5	6.2	3.0	4.1
Eu	0.5	0.8	0.6	0.7	1.0	0.1	0.6	1.5	1.3	bdl	0.5	0.4	0.4	1.6	0.4	1.2	1.0

Table 3 (continued)

Sample	018	020[a]	031	032[a]	236	238[a]	242	258[a]	260[a]	266	267[a]	273	283	330	331[a]	342[a]	343[a]
Gd	1.4	2.2	1.0	1.9	3.5	0.05	2.1	4.7	5.3	1.2	1.1	1.6	3.0	5.2	6.9	3.5	4.6
Tb	0.1	0.2	0.1	0.3	0.4	0.01	0.2	0.6	0.8	bdl	0.2	bdl	bdl	1.0	1.2	0.6	0.8
Dy	0.7	1.0	0.8	1.8	3.1	0.05	1.4	2.7	4.9	bdl	1.1	bdl	0.9	4.9	7.4	3.6	5.5
Ho	0.1	0.2	0.1	0.4	0.6	0.01	0.2	0.5	1.0	bdl	0.2	0.4	0.2	1.1	1.6	0.7	1.2
Er	bdl	0.5	0.6	1.0	1.9	0.03	0.6	1.4	2.8	bdl	0.6	bdl	bdl	1.5	4.9	2.1	3.9
Tm	bdl	0.1	0.1	0.1	0.2	0.00	0.2	0.2	0.4	bdl	0.1	bdl	bdl	0.4	0.8	0.3	0.6
Yb	bdl	0.3	0.7	0.8	1.6	0.03	1.3	1.2	2.4	bdl	0.5	bdl	bdl	3.9	4.8	1.9	4.1
Lu	bdl	0.1	0.1	0.1	0.2	0.00	0.2	0.2	0.4	bdl	0.1	bdl	bdl	0.5	0.7	0.3	0.7
Hf	2.5	1.6	4.1	0.5	1.6	0.2	5.9	1.6	1.2	3.3	0.2	bdl	3.1	5.8	3.7	2.2	3.8
Ta	0.1	0.5	0.2	0.2	0.3	bdl	2.0	1.8	1.0	0.8	0.2	0.9	0.3	1.8	3.6	0.6	0.5
Pb	5.9	18.6	2.3	26.4	1.0	6.5	3.2	19.7	9.3	6.6	9.2	21.2	5.9	9.4	9.4	3.5	2.4
Th	3.3	14.7	3.2	6.2	0.9	0.0	25.6	8.1	5.0	5.8	0.3	10.9	11.6	4.3	17.0	1.6	4.4
U	0.9	1.5	0.8	1.1	0.3	0.0	3.3	2.4	1.7	1.8	0.5	3.9	2.0	1.3	2.5	0.4	1.2
$^{87}Sr/^{86}Sr_{(i)}$		0.704215		0.707338		0.706974		0.704567	0.706309		0.705354				0.703161	0.704121	0.703252
$^{143}Nd/^{144}Nd_{(i)}$		0.512406		0.512212		–		0.512406	0.512385		0.512196				0.512545	0.512707	0.512695

[a]Samples analyzed by solution ICP–MS for sample locations see Fig. 2 or coordinates in Table 1

[b]Fe_2O_3: total iron

[c]LOI: loss on ignition

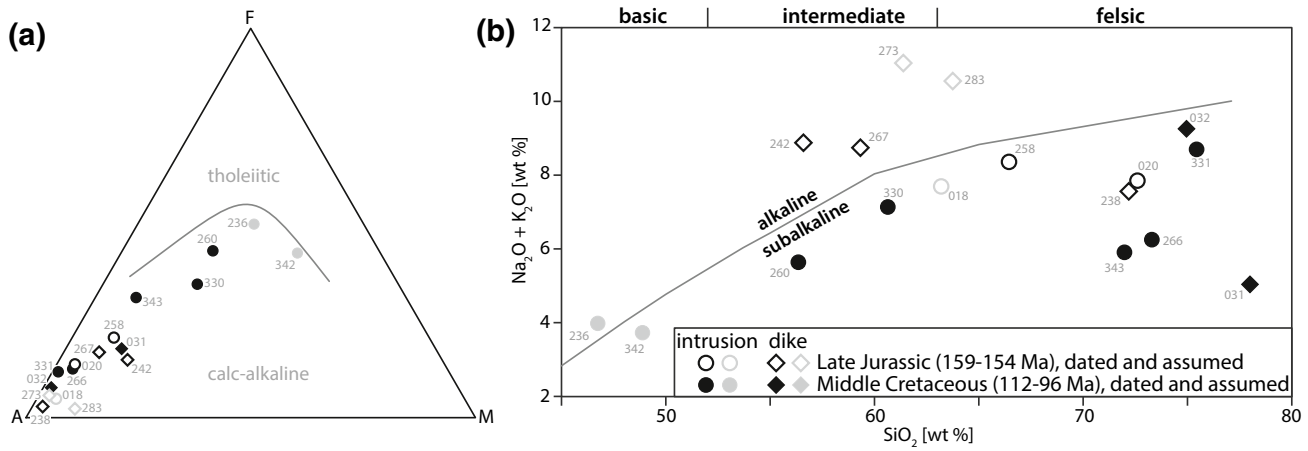

Fig. 5 **a** AFM (A = $Na_2O + K_2O$, F = FeO_{tot}, M = MgO) diagram with calc-alkaline–tholeiitic boundary after Irvine and Baragar (1971). **b** Total alkali vs. SiO_2 diagram (Middlemost 1994)

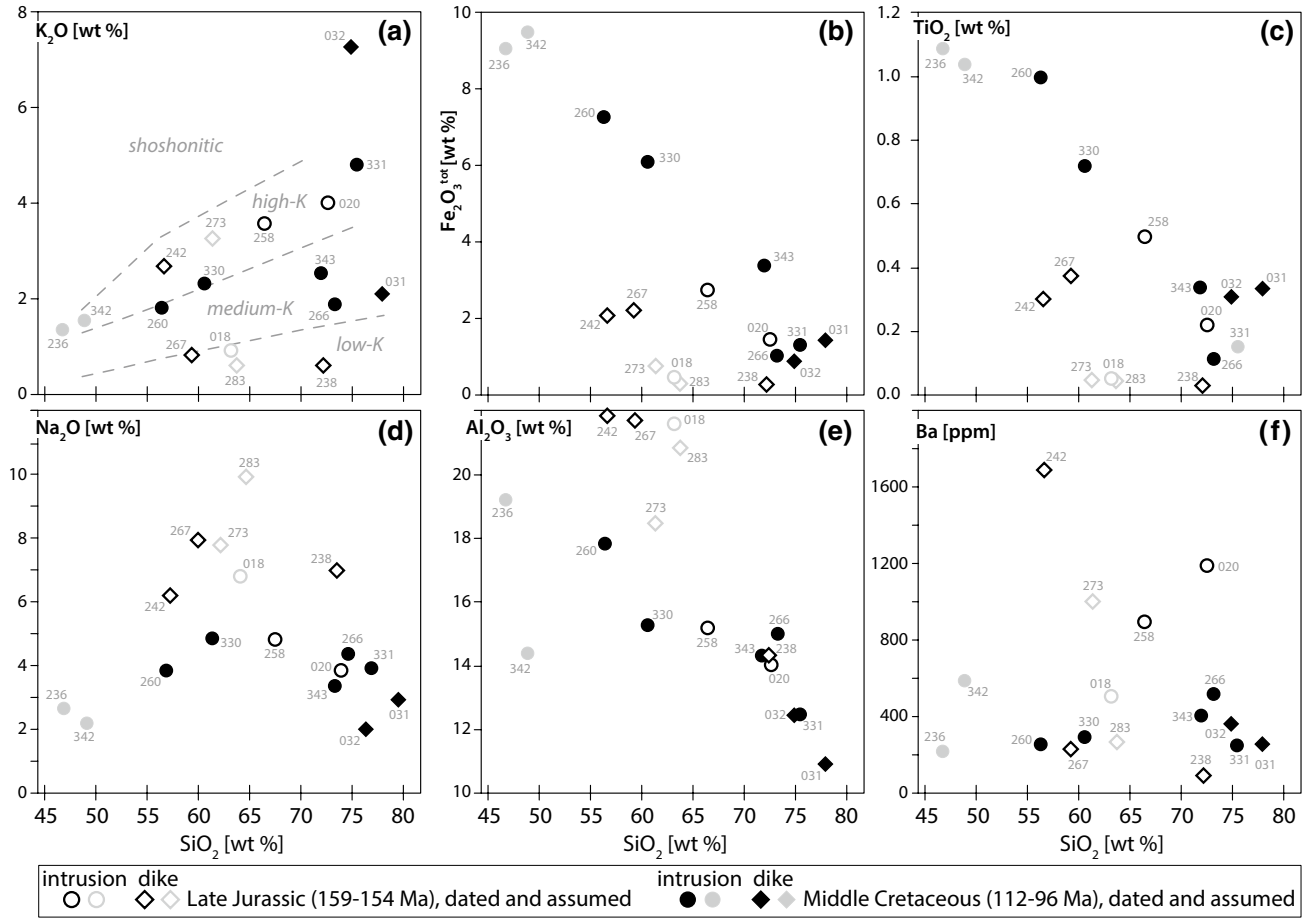

Fig. 6 Bulk rock major element compositions. **a** K_2O vs. SiO_2. **b** $Fe_2O_3^{tot}$ vs. SiO_2. **c** TiO_2 vs. SiO_2. **d** Na_2O vs. SiO_2. **e** Al_2O_3 vs. SiO_2. **f** MnO vs. SiO_2

and Ba (Fig. 6a, f; $K_2O < 0.8$ wt% or $K_2O > 2.7$ wt%; Ba = 200–1700 ppm). Chondrite-normalized rare earth element (REE_N) diagrams of Late Jurassic samples (Fig. 7a) are also very variable. One group of patterns is characterized by fractionated light REE (LREE) and heavy REE (HREE) (e.g. $(La/Yb)_N > 25$) with medium LREE concentrations

(< 100 times chondrite concentrations) and low abundance of HREE (2–7 times chondrite concentrations). Incompatible large ion lithophile elements (LILE; e.g. Rb, Ba, Sr) are enriched while high-field strength elements (HFSE; e.g. Nb, Ta, Zr and Hf) compared to LILE are slightly depleted (Fig. 7b). The second group of REE patterns is flat [$(La/Yb)_N = 3–5$] with positive Eu anomalies indicating plagioclase accumulation. Trondhjemite dike 238 is strongly depleted in REE concentrations (< 1 chondrite concentration). N-MORB-normalized trace element variation diagrams show enrichment in LILE Ba and Sr consistent with plagioclase accumulation.

Middle Cretaceous samples plot in the sub-alkaline field. They are characterized by negative correlation of major oxides such as $Fe_2O_3^{tot}$, TiO_2, Al_2O_3 (Fig. 6) and MnO, CaO and MgO (not plotted) with silica content. LREE and HREE are slightly to moderately fractionated [e.g. $(La/Yb)_N = 2–10$]. The patterns differ from each other in the extent of the Eu anomaly (Fig. 7c). Samples 032 and 342 exhibit a small positive Eu anomaly indicating moderate plagioclase accumulation. Samples 260 and 343 have a slight and 331 a marked negative Eu anomaly indicating plagioclase fractionation from the parental magma. N-MORB-normalized trace element variation diagrams show enrichment in LILE and moderate negative Nb–Ta and Ti anomalies, suggesting a source that was modified by melts or fluids coexisting with a TiO_2-rich phase such as rutile, ilmenite or titanite (Fig. 7d).

Radiogenic isotope geochemistry

Nine selected rock powders have been analyzed for Sr and Nd isotopic compositions (Fig. 8) at Victoria University of Wellington. Results were back calculated to initial isotopic ratios (Table 3). Standard compositions and standard deviations are described in supplementary Table S7.

Initial Sr isotopic ratios ($^{87}Sr/^{86}Sr_{(i)}$) of Jurassic samples range from 0.704215 to 0.705354. Initial Nd isotopic ratios are low with $^{143}Nd/^{144}Nd_{(i)}$ ranging from 0.512196 to 0.512406. No $^{143}Nd/^{144}Nd$ values could be obtained for

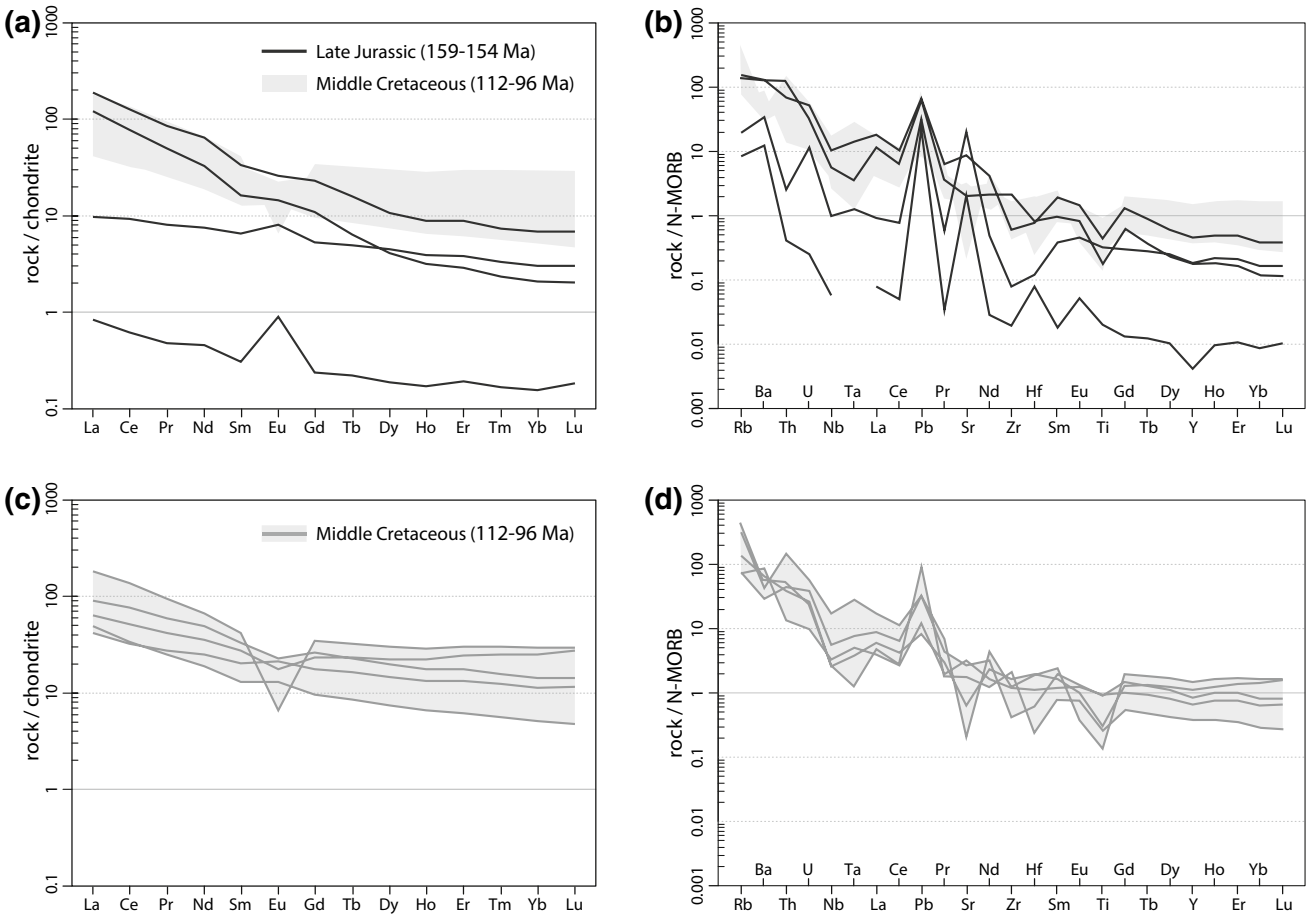

Fig. 7 **a, c** Chondrite-normalized REE concentrations after McDonough and Sun (1995) and **b, d** N-MORB-normalized trace element plots after Sun and McDonough (1989) for representative granitoids. The plotted trace element data were exclusively obtained by solution ICP–MS. Shaded areas represent the compositional field of Middle Cretaceous samples

Jurassic dike 238 ($^{87}Sr/^{86}Sr_{(i)} = 0.706974$) due to very low Nd concentrations. Cretaceous samples show a wider range for both $^{87}Sr/^{86}Sr_{(i)}$ (0.703161–0.707338) and $^{143}Nd/^{144}Nd_{(i)}$ (0.512212–0.512707). Plotting the $\varepsilon Nd_{(i)}$ against the age of the samples (Fig. 8 inset) shows that Jurassic samples are restricted to negative $\varepsilon Nd_{(i)}$ values (−4.7 to −0.5), overlapping with Cretaceous $\varepsilon Nd_{(i)}$ values (−5.6 to +4).

Discussion

Fieldwork and zircon ages revealed an uneven distribution of Mesozoic magmatic rocks in space and time (Fig. 2). Late Jurassic samples could be dated on both sides of the Siah Cheshmeh–Khoy right lateral strike-slip fault, suggesting an analogous tectono-magmatic evolution during this time for the two sides of the fault, i.e. WMU and EKOC + CIB. Cretaceous samples occur only on the Central Iranian block, northeastern side of the fault. This space and time distribution requires discussion of the petrogenetic and tectonic significance of these magmatic populations.

Petrogenesis and magma source

Late Jurassic samples are characterized by low concentrations of $Fe_2O_3^{tot}$ and TiO_2 (Fig. 6) indicating that the composition of these intermediate to acidic alkaline magmas was modified by early ilmenite fractionation. These samples can be subdivided into alkaline and sub-alkaline rocks (Fig. 5). Differences in alkalinity indicate different sources and/or variable degrees of partial melting and/or H_2O contents of the primary magmas.

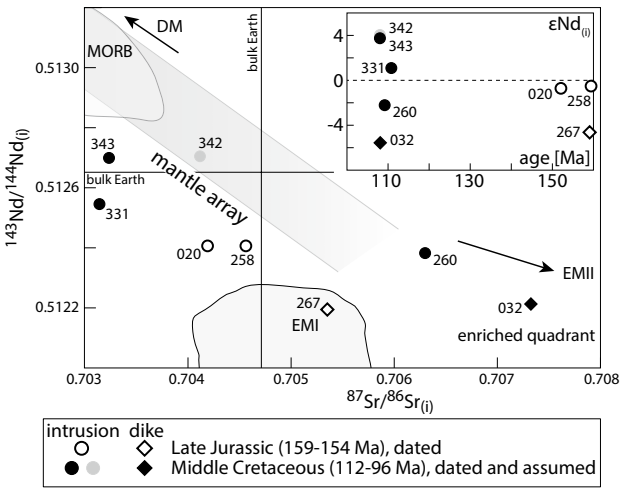

Fig. 8 Plot of $^{143}Nd/^{144}Nd_{(i)}$ versus $^{87}Sr/^{86}Sr_{(i)}$. For sample locations see Fig. 2. Mantle reservoirs (*DM* depleted mantle, *EMI and EMII* enriched mantle) from Zindler and Hart (1986), bulk Earth (BSE) after Allègre et al. (1979), mantle array as used in Rollinson (1993) and MORB from Hofmann (2003)

The alkaline samples are characterized by relatively high X_{Mg} values [$0.45 < X_{Mg} < 0.67$ with one outlier at 0.89 (sample 283 with extremely low Fe_2O_3)] for their, respectively, high silica contents (56–64 wt%) which is a consequence of (1) early Fe–Ti-oxide saturation effectively depleting Fe along the liquid line of descent and (2) their alkaline character expressed by lower SiO_2 content at comparable extent of differentiation. Alkaline samples 242 and 273 are enriched in incompatible elements, such as K and Ba (Fig. 6a, f) emphasizing their highly evolved character despite their intermediate silica content. This clearly points towards an alkaline magma evolution. Inherited zircons may indicate crustal contamination, but since sample 242 delivered only one zircon grain and sample 273 remains undated, the enrichment in incompatible elements cannot unambiguously be ascribed to crustal contamination. On the other hand, alkaline samples 267 and 283 have low concentrations of incompatible elements, such as K, Ba and Rb (Fig. 6a, f), which is inconsistent with derivation from a mica-rich crustal source. The high $^{87}Sr/^{86}Sr_{(i)}$ ratio of 0.706973 and negative $\varepsilon Nd_{(i)}$ value of −4.7 in sample 267 is derived either from an enriched mantle source or from interaction with ancient crustal material (AFC—assimilation–fractional–crystallization) in deep seated magma reservoirs (Fig. 8). Inherited Paleoproterozoic to Early Jurassic zircon cores indicate that sample 267 experienced crustal contamination during differentiation, ascent and emplacement. Trace element variation diagrams reveal a rather flat pattern with only moderate enrichment of LREE (Fig. 7) which can either be attributed to fractionation of REE-rich accessories, such as titanite and allanite (a well-known feature in highly differentiated magmas, e.g. Bea 1996; Miller and Mittlefehldt 1982) or their derivation by partial melting from a LREE-poor source such as mafic granulites (e.g. Bea and Montero 1999).

The Jurassic sub-alkaline samples 020 and 258 with low $^{87}Sr/^{86}Sr_{(i)}$ ratios (0.704215–0.704567) and $\varepsilon Nd_{(i)}$ values close to 0 (−0.5 to −0.7) indicate a mantle-dominated source (Fig. 8). However, these samples are enriched in LREE and LILE, depleted in HREE and have negative Nb–Ta and Ti anomalies, which are common features in granites involving partial melting of the continental crust (Fig. 7; e.g. Pearce and Peate 1995). The enrichment in incompatible elements and the presence of inherited cores and assimilated zircon grains in these samples is consistent with crustal contamination during ascent and emplacement of the magmas. The Paleoproterozoic to Early Jurassic inherited cores match ages from the Central Iranian basement and its Mesozoic cover (Hassanzadeh et al. 2008). These intrusions were emplaced in close vicinity to Late Jurassic sediments cropping out to the north east of the field area (Majidi et al. 2007). This vicinity suggests that the granites reached

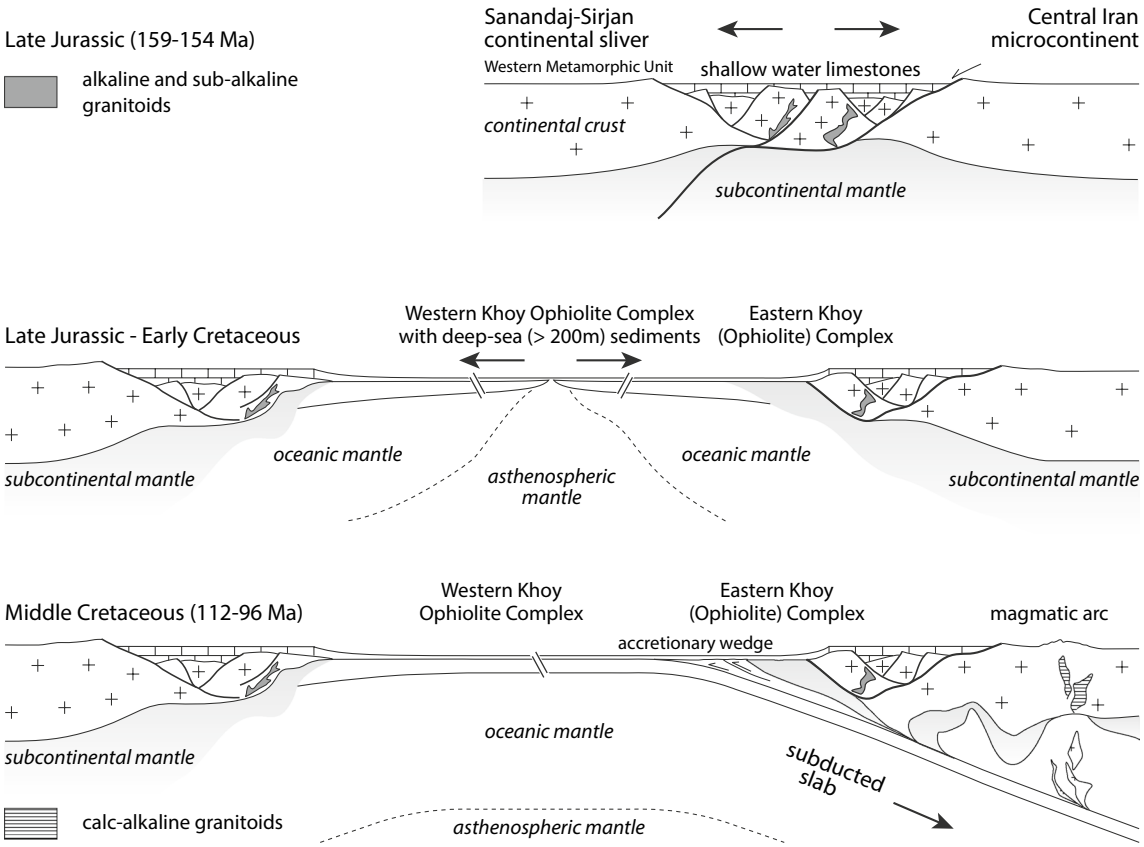

Fig. 9 Schematic tectonic interpretation (not to scale) from Late Jurassic to Middle Cretaceous for NW Iranian Azerbaijan

shallow crustal levels, close to the sedimentary cover of the same age.

Middle Cretaceous samples show negative trends for $Fe_2O_3^{tot}$, TiO_2, Al_2O_3, MnO, CaO and MgO with increasing silica content (Fig. 6). These trends could be interpreted as differentiation characteristics originating from a common parental melt. However, isotopic results with highly variable $^{87}Sr/^{86}Sr_{(i)}$ (0.703252–0.707338) and $\varepsilon Nd_{(i)}$ from −5.6 to +4 indicate either different magma sources or significant interaction with crustal lithologies during crystallization-differentiation (Fig. 8). Samples 331, 342 and 343 have positive $\varepsilon Nd_{(i)}$ values (+1 to +4) lying close or within the mantle array, hence indicating dominance of a mantle source. Samples 032 and 260 with negative $\varepsilon Nd_{(i)}$ values (−5.6 and −2.2) and high $^{87}Sr/^{86}Sr_{(i)}$ indicate an enriched contribution to the melt, either source inherited or acquired by crustal assimilation. Inherited zircon cores point to crustal contamination during differentiation, ascent and emplacement of the magmas. Trace elements characterized by elevated LILE concentrations, and negative Nb–Ta and Ti anomalies are typical for arc-related magmatic rocks (Fig. 7; e.g. Pearce and Peate 1995). Fluids released from the slab during subduction reduce the melting point, thus enable significant partial melting of the mantle wedge (e.g. Tatsumi 1986). This is in accordance with the larger amount of hydrous minerals and higher LOI values in the Cretaceous samples than in Jurassic samples.

The dominantly 159–155 and 112–104 $^{40}K/^{40}Ar$ and $^{40}Ar/^{39}Ar$ ages of hornblendes from EKOC amphibolites (Ghazi et al. 2001, 2003; Khalatbari-Jafari et al. 2004; Pessagno et al. 2005) are coeval with the Cretaceous intrusion ages obtained in this work and thus likely record thermal events caused by Cretaceous magmatism.

Tectonic evolution of the Khoy area

With the aid of field and satellite mapping, bulk rock geochemistry, and zircon dating, the Mesozoic tectonic and magmatic evolution of the Khoy area can be reconstructed (Fig. 9).

In the Late Jurassic, alkaline mantle-derived melts intruded the Precambrian basement covered by Permo-Triassic platform limestones (Amini et al. 1993; Aminiazar and Abbasi 2003; Khodabandeh et al. 2002a; Radfar et al. 1993). The transition from shallow water shelf deposits into thinly

bedded limestones with Late Jurassic benthic foraminifera and microfossils, and chert nodules in the upper sequence (Majidi et al. 2007) indicate deepening of the sedimentary environment, hence subsidence. This regional subsidence is coeval with the alkaline–sub-alkaline intrusions dated in this study. Coeval magmatism and subsidence denote lithospheric thinning of the Central Iranian continental block with the Khoy area representing its continental margin. Possible causes for continental rifting are mantle plume activity and passive rifting. The mantle source is inconsistent with upwelling of a deep asthenospheric source, which would produce suites ranging from strongly alkali-, incompatible element-enriched (Pearce 1996) to transitional tholeiitic magmas unlike the obtained analyses of Jurassic samples. Therefore, we favor passive rifting where magmatism is due to decompression of a variably metasomatized subcontinental lithosphere. These melts experienced various degrees of crustal contamination during differentiation, ascent and emplacement into the thinning continental crust, generating alkaline to sub-alkaline compositions. The mantle signatures testified by the isotope geochemistry and the presence of inherited cores in dated Jurassic zircons are both compatible with this interpretation. NNE–SSW to NE–SW striking dikes suggest ESE–WNW to SE–NW directed extension. Asymmetric passive rifting would explain exhumation of the subcontinental lithospheric mantle of the Central Iran block, now preserved as the eastern Khoy 'ophiolite' complex. Further extension led oceanic spreading and the formation of the oceanic lithosphere now partly preserved in the Western Khoy ophiolite complex.

Mid-Cretaceous intrusions with arc signatures suggest subduction of the Early Cretaceous oceanic lithosphere below the Central Iranian margin. Early Cretaceous sediments are found only as latest Albian to early Cenomanian (< 100 Ma; Ghazi et al. 2003; Pessagno et al. 2005) olistoliths in the Campanian olistostrome of the study area (Avagyan et al. 2017). We contend that the most part of these sediments has been subducted with the ocean floor (the non-metamorphic WKOC). The planktonic foraminiferae and radiolarian assemblages of these sediments indicate a deep-sea environment in the Khoy oceanic basin during the Early Cretaceous.

We interpret the 40-Ma age gap between the Late Jurassic and the Middle Cretaceous magmatic episodes as the time of existence of the Khoy oceanic basin. The Early Cretaceous magmatic gap is reported all along the Urumieh–Dokhtar magmatic arc and the Sanandaj–Sirjan zone (Chiu et al. 2013). It has been explained by migration of the magmatic arc from the Jurassic Sanandaj–Sirjan zone to the Tertiary Urumieh–Dokhtar magmatic arc (Agard et al. 2011; Verdel et al. 2011). This migration would be caused by the conjectural flattening of the Neo-Tethyan subduction angle. However, this interpretation is at odds with the geochemical signatures of Jurassic intrusions while the sedimentation environment was deepening (e.g. Hunziker et al. 2015; Mohammadi et al. 2016; Şengör 1990). Jurassic subduction along the southwest border of the Sanandaj–Sirjan zone was mainly inferred from a 'subduction' signature with LILE- and LREE-enriched, and HFSE-depleted patterns in granitoids (e.g. Azizi et al. 2015; Bayati et al. 2017; Chiu et al. 2013; Esna-Ashari et al. 2012; Ghasemi and Talbot 2006; Khalaji et al. 2007; Mahmoudi et al. 2011; Mohajjel and Fergusson 2014; Mohajjel et al. 2003). However, geotectonic classifications of granitoids should be used with caution as several types of contemporaneous granitoids may occur together in the same tectonic setting (Barbarin 1990). This ambiguity is particularly true for the trace element chemistry, which is sensitive to minor (accessory) phases, mixed sources, volatile interaction, variable degrees of partial melting, and restite accumulation (Winter 2010). We suggest that the inferred, Jurassic 'subduction' signature is rather a consequence of either (1) the derivation of the primary magmas from an enriched, previously metasomatized mantle source (e.g. by ancient subduction events) or (2) the assimilation/contamination of the mantle-derived magmas by continental crust during differentiation, storage and ascent.

An open question remains the change from opening to closure of the Khoy oceanic basin. The Middle Cretaceous rhyodacite and granitoids have calc-alkaline characteristics of a rather mature arc. For comparison, it took < 10 Ma from subduction initiation to calc-alkaline arc magmatism in the reference Izu–Bonin–Mariana forearc (e.g. Ishizuka et al. 2011). If this estimate is applied to the Khoy area, subduction of the Khoy oceanic basin started approximately 120 Ma ago.

Correlations with similar tectonic units in Turkey (e.g. Ağrı, Maku, Siah Cheshmeh and Van) remain unclear. Along with the Khoy ophiolite, the border region between Turkey and Iran is characterized by ophiolites and ophiolitic mélanges. Basement rocks in Turkey are mainly represented by Late Cretaceous, high-temperature/low-pressure metamorphic rocks. Jurassic igneous and metamorphic rocks are unknown (e.g. Oberhänsli et al. 2010; Topuz et al. 2017). Based on the striking differences between Eastern Turkey and NW Iran, Şengör (1990) and Topuz et al. (2017) connect the Izmir–Ankara–Erzincan suture with the Zagros suture. More fieldwork and analytical studies are necessary to corroborate such an interpretation.

Conclusion

Zircon dating of magmatic rocks in the Khoy area revealed two, ca. 40-Ma-apart periods of magmatic activity. Late Jurassic (159–154 Ma) magmatism took place during

continental rifting, which separated the Central Iran block to the northwest from the Sanandaj–Sirjan continental sliver to the southeast. Geochemical analyses suggest a mantle-dominated source for these magmas, which were variably affected by crustal contamination during differentiation, ascent and emplacement in a thinning, subsiding crust. This rifting event preceded the Early Cretaceous formation of the non-metamorphic Khoy ophiolite in an oceanic basin between the Sanandaj–Sirjan zone and the Central Iranian block. Mid-Cretaceous (112–96 Ma) magmatism indicates subduction of the Khoy basin below the Central Iranian margin. Subduction of this basin beneath the Central Iranian block may have started ca 120 Ma ago. The active Siah Cheshmeh–Khoy Fault has reactivated the former suture.

Acknowledgements This research was financially supported by SNF Research Grant (project 2-77979-14). Remy Lüchinger prepared thin sections, Lydia Zehnder helped with the XRF analyses, Markus Wälle with the LA–ICP–MS and Karsten Kunze with the CL and BSE imaging of zircons. Albrecht von Quadt provided secondary zircon reference material. Thanks to Bruce Charlier from Victoria University Wellington for the isotope measurements and the help on the related methodological part. Logistic support from the Geological Survey of Iran is appreciated. We thank Gültekin Topuz and Axel Schmitt for detailed and valuable comments and Jochen Hoefs for the editorial work.

Compliance with ethical standards

Conflict of interest The authors declare that they have no conflict of interest.

Data availability Associated data to this article are found in the supplements S1–S7.

References

Agard P, Omrani J, Jolivet L, Mouthereau F (2005) Convergence history across Zagros (Iran): constraints from collisional and earlier deformation. Int J Earth Sci 94:401–419

Agard P, Omrani J, Jolivet L, Whitechurch H, Vrielynck B, Spakman W, Monié P, Meyer B, Wortel R (2011) Zagros orogeny: a subduction-dominated process. Geol Mag 148:692–725

Allègre CJ, Othman DB, Polve M, Richard P (1979) The Nd-Sr isotopic correlation in mantle materials and geodynamic consequences. Phys Earth Planet Inter 19:293–306

Amini B, Radfar J, Khalatbari M, Bahroudi A (1993) Dizaj geological quadrangle map: 1:100,000. Geol Surv Iran

Aminiazar R, Abbasi S (2003) Maku geological quadrangle map: 1:100,000. Geol Surv Iran

Avagyan A, Shahidi A, Sosson M, Sahakyan L, Galoyan G, Muller C, Vardanyan S, Firouzi KB, Bosch D, Danelian T, Asatryan G, Mkrtchyan M, Shokri MA (2017) New data on the tectonic evolution of the Khoy region, NW Iran. Geol Soc Lond Spec Publ 428:99–116

Azizi H, Chung S-L, Tanaka T, Asahara Y (2011) Isotopic dating of the Khoy metamorphic complex (KMC), northwestern Iran: a significant revision of the formation age and magma source. Precambrian Res 185:87–94

Azizi H, Zanjefili-Beiranvand M, Asahara Y (2015) Zircon U–Pb ages and petrogenesis of a tonalite-trondhjemite-granodiorite (TTG) complex in the northern Sanandaj-Sirjan zone, northwest Iran: Evidence for Late Jurassic arc-continent collision. Lithos 216:178–195

Ballato P, Uba CE, Landgraf A, Strecker MR, Sudo M, Stockli D, Friedrich A, Tabatabaei SH (2011) Arabia–Eurasia continental collision: insights from late Tertiary foreland basin evolution in the Alborz Mountains, northern Iran. Geol Soc Am Bull 123:106–131

Barbarin B (1990) Granitoids: main petrogenetic classifications in relation to origin and tectonic setting. Geol J 25:227–238

Barker F (1979) Trondhjemite: definition, environment and hypothesis of origin. In: Barker F (ed) Trondhjemites, dacites, and related rocks. Elsevier, Amsterdam, pp 1–12

Bayati M, Esmaeily D, Maghdour-Mashhour R, Li X-H, Stern RJ (2017) Geochemistry and petrogenesis of Kolah-Ghazi granitoids of Iran: Insights into the Jurassic Sanandaj-Sirjan magmatic arc. Chem Erde-Geochem 77:281–302

Bea F (1996) Residence of REE, Y, Th and U in granites and crustal protoliths; implications for the chemistry of crustal melts. J Petrol 37:521–552

Bea F, Montero P (1999) Behavior of accessory phases and redistribution of Zr, REE, Y, Th and U during metamorphism and partial melting of metapelites in the lower crust: an example from the Kinzigite Formation of Ivrea-Verbano, NW Italy. Geochim Cosmochim Acta 63:1133–1153

Berberian M, King G (1981) Towards a paleogeography and tectonic evolution of Iran. Can J Earth Sci 18:210–265

Chiu H-Y, Chung S-L, Zarrinkoub MH, Mohammadi SS, Khatib MM, Iizuka Y (2013) Zircon U–Pb age constraints from Iran on the magmatic evolution related to Neotethyan subduction and Zagros orogeny. Lithos 162–163:70–87

Djamour Y, Vernant P, Nankali HR, Tavakoli F (2011) NW Iran-eastern Turkey present-day kinematics: results from the Iranian permanent GPS network. Earth Planet Sci Lett 307:27–34

Esna-Ashari A, Tiepolo M, Valizadeh M-V, Hassanzadeh J, Sepahi A-A (2012) Geochemistry and zircon U–Pb geochronology of Aligoodarz granitoid complex, Sanandaj-Sirjan zone, Iran. J Asian Earth Sci 43:11–22

Ghasemi A, Talbot CJ (2006) A new tectonic scenario for the Sanandaj-Sirjan Zone (Iran). J Asian Earth Sci 26:683–693

Ghazi M, Pessagno E, Hassanipak A, Kariminia M, Campbell K (2001) Tectonogenesis of the Khoy ophiolite, NW Iran: results from biostratigraphic/chronostratigraphic and $^{40}Ar/^{39}Ar$ studies. In: International Conference of the Geology of Oman, Abstract Volume, Sultan Qaboos University, Oman, pp 34–35

Ghazi AM, Pessagno EA, Hassanipak AA, Kariminia SM, Duncan RA, Babaie HA (2003) Biostratigraphic zonation and $^{40}Ar–^{39}Ar$ ages for the Neotethyan Khoy ophiolite of NW Iran. Palaeogeogr Palaeocl 193:311–323

Guest B, Stockli DF, Grove M, Axen GJ, Lam PS, Hassanzadeh J (2006) Thermal histories from the central Alborz Mountains, northern Iran: implications for the spatial and temporal distribution of deformation in northern Iran. Geol Soc Am Bull 118:1507–1521

Haghipour A, Eftekhar-Nezhad J, Ghorashi M, Arshadi S (1978) Khoy geological quadrangle map: 1:250′000. Geol Surv Iran

Hassanzadeh J, Wernicke BP (2016) The Neotethyan Sanandaj-Sirjan zone of Iran as an archetype for passive margin-arc transitions. Tectonics 35:586–621

Hassanzadeh J, Stockli DF, Horton BK, Axen GJ, Stockli LD, Grove M, Schmitt AK, Walker JD (2008) U–Pb zircon geochronology of late Neoproterozoic-Early Cambrian granitoids in Iran: implications for paleogeography, magmatism, and exhumation history of Iranian basement. Tectonophysics 451:71–96

Hofmann AW (2003) Sampling mantle heterogeneity through oceanic basalts: isotopes and trace elements. Treatise Geochem 2:1–44

Horstwood MSA, Košler J, Gehrels G, Jackson SE, McLean NM, Paton C, Sircombe K, Sylvester P, Vermeesch P, Bowring JF, Condon DJ, Schoene B (2016) Community-derived standards for LA-ICP-MS U-(Th-)Pb geochronology—uncertainty propagation, age interpretation and data reporting. Geostand Geoanal Res 40:311–332

Hunziker D, Burg J-P, Bouilhol P, von Quadt A (2015) Jurassic rifting at the Eurasian Tethys margin: geochemical and geochronological constraints from granitoids of North Makran, southeastern Iran. Tectonics 34:571–593

Irvine TN, Baragar WRA (1971) A guide to the chemical classification of the common volcanic rocks. Can J Earth Sci 8:523–548

Ishizuka O, Tani K, Reagan MK, Kanayama K, Umino S, Harigane Y, Sakamoto I, Miyajima Y, Yuasa M, Dunkley DJ (2011) The timescales of subduction initiation and subsequent evolution of an oceanic island arc. Earth Planet Sc Lett 306:229–240

Karakhanian AS, Trifonov VG, Philip H, Avagyan A, Hessami K, Jamali F, Bayraktutan MS, Bagdassarian H, Arakelian S, Davtian V (2004) Active faulting and natural hazards in Armenia, eastern Turkey and northwestern Iran. Tectonophysics 380:189–219

Khalaji AA, Esmaeily D, Valizadeh M, Rahimpour-Bonab H (2007) Petrology and geochemistry of the granitoid complex of Boroujerd, Sanandaj-Sirjan Zone, Western Iran. J Asian Earth Sci 29:859–877

Khalatbari-Jafari M, Juteau T, Bellon H, Emami H (2003) Discovery of two ophiolite complexes of different ages in the Khoy area (NW Iran). C R Geosci 335:917–929

Khalatbari-Jafari M, Juteau T, Bellon H, Whitechurch H, Cotten J, Emami H (2004) New geological, geochronological and geochemical investigations on the Khoy ophiolites and related formations, NW Iran. J Asian Earth Sci 23:507–535

Khodabandeh A, Soltani G, Sartipi A, Emami MH (2002a) Qotour geological quadrangle map: 1:100,000, Geol Surv Iran

Khodabandeh A, Soltani G, Sartipi A, Emami MH (2002b) Salmas geological quadrangle map: 1:100,000. Geo Surv Iran

Lam PS (2002) Geology, geochronology, and thermochronology, of the Alam Kuh Area, Central Alborz Mountains, Northern Iran. University of California, Los Angeles

Le Maitre RW, Streckeisen A, Zanettin B, Le Bas ML, Bonin B, Bateman P, Bellieni G, Dudek A, Efremova J, Keller J, Lameyre J, Sabine PA, Schmid R, Sorenson H, Wooley AR (2002) Igneous rocks: a classification and glossary of terms. Cambridge University Press, Cambridge

Ludwig K (2012) User's manual for Isoplot version 3.75–4.15: a geochronological toolkit for Microsoft. Excel Berkeley Geochronological Center Special Publication, Berkeley

Mahmoudi S, Corfu F, Masoudi F, Mehrabi B, Mohajjel M (2011) U–Pb dating and emplacement history of granitoid plutons in the northern Sanandaj-Sirjan Zone, Iran. J Asian Earth Sci 41:238–249

Majidi J, Ghalamghash J, Babakani AR (2007) Siahcheshmeh geological quadrangle map: 1:100,000. Geol Surv Iran

Mattinson JM (2005) Zircon U–Pb chemical abrasion ("CA-TIMS") method: combined annealing and multi-step partial dissolution analysis for improved precision and accuracy of zircon ages. Chem Geol 220:47–66

McDonough WF, Sun S-S (1995) The composition of the Earth. Chem Geol 120:223–253

Middlemost EAK (1994) Naming materials in the magma/igneous rock system. Earth-Sci Rev 37:215–224

Miller CF, Mittlefehldt DW (1982) Depletion of light rare-earth elements in felsic magmas. Geology 10:129–133

Mohajjel M, Fergusson C (2014) Jurassic to Cenozoic tectonics of the Zagros Orogen in northwestern Iran. Int Geol Rev 56:263–287

Mohajjel M, Fergusson C, Sahandi M (2003) Cretaceous-Tertiary convergence and continental collision, Sanandaj-Sirjan zone, western Iran. J Asian Earth Sci 21:397–412

Mohammadi A, Burg J-P, Winkler W (2016) Detrital zircon and provenance analysis of Eocene-Oligocene strata in the South Sistan suture zone, southeast Iran: implications for the tectonic setting. Lithosphere L538-1

Oberhänsli R, Candan O, Bousquet R, Rimmele G, Okay AI, Goff BJ (2010) Alpine HP evolution of the eastern Bitlis complex, SE Turkey. In: Sosson M, Kaymakçı N, Stephenson R, Starostenko V, Bergerat F (eds) Sedimentary basin tectonics from the Black Sea and Caucasus to the Arabian Platform, vol 340. Geol Soc Lond Spec Publ, London, pp 461–483

Okay AI, Zattin M, Cavazza W (2010) Apatite fission-track data for the Miocene Arabia–Eurasia collision. Geology 38:35–38

Pearce J (1996) Sources and settings of granitic rocks. Episodes 19:120–125

Pearce JA, Peate DW (1995) Tectonic implications of the composition of volcanic arc magmas. Annu Rev Earth Planet Sci 23:251–285

Pessagno EA, Ghazi AM, Kariminia M, Duncan RA, Hassanipak AA (2005) Tectonostratigraphy of the Khoy Complex, northwestern Iran. Stratigraphy 2:49–63

Radfar J, Amini B, Bahroudi A, Khalatbari M, Emami MH (1993) Khoy geological quadrangle map: 1:100,000. Geol Surv Iran

Ramezani J, Tucker RD (2003) The Saghand region, central Iran: U–Pb geochronology, petrogenesis and implications for Gondwana tectonics. Am J Sci 303:622–665

Rollinson HR (1993) Using geochemical data: evaluation, presentation, interpretation. Longman, London

Samani B, Zhuyi G, Xuetao G, Chuan T (1994) Geology of Precambrian in Central Iran; on the context of stratigraphy, magmatism and metamorphism. Geosci Quart 3:40–63

Şengör AMC (1990) A new model for the late Palaeozoic-Mesozoic tectonic evolution of Iran and implications for Oman. Geol Soc Lond Spec Publ 49:797–831

Stampfli GM (2000) Tethyan oceans. Geol Soc Lond Spec Publ 173:1–23

Stöcklin J (1968) Structural history and tectonics of Iran: a review. Am Assoc Petrol Geol Bull 52:1229–1258

Sun S-S, McDonough W-s (1989) Chemical and isotopic systematics of oceanic basalts: implications for mantle composition and processes. Geol Soc Lond Spec Publ 42:313–345

Tatsumi Y (1986) Formation of the volcanic front in subduction zones. Geophys Res Lett 13:717–720

Topuz G, Candan O, Zack T, Yılmaz A (2017) East Anatolian Plateau constructed over a continental basement: no evidence for the East Anatolian Accretionary Complex. Geology 45:791–794

Verdel C, Wernicke BP, Ramezani J, Hassanzadeh J, Renne PR, Spell TL (2007) Geology and thermochronology of Tertiary Cordilleran-style metamorphic core complexes in the Saghand region of central Iran. Geol Soc Am Bull 119:961–977

Verdel C, Wernicke BP, Hassanzadeh J, Guest B (2011) A Paleogene extensional arc flare-up in Iran. Tectonics 30:TC3008

Vincent SJ, Allen MB, Ismail-Zadeh AD, Flecker R, Foland KA, Simmons MD (2005) Insights from the Talysh of Azerbaijan into the Paleogene evolution of the South Caspian region. Geol Soc Am Bull 117:1513–1533

Whitney DL, Evans BW (2010) Abbreviations for names of rock-forming minerals. Am Mineral 95:185

Winter JD (2010) An introduction to igneous and metamorphic petrology. Prentice Hall, New York

Zindler A, Hart S (1986) Chemical geodynamics. Annu Rev Earth Pl Sc 14:493–571